J. Fluid Mech. (2000), *vol.* 404, *pp.* 87–115. Printed in the United Kingdom

Dynamics of a low Reynolds number turbulent boundary layer

By JUAN M. CHACIN[1]† AND BRIAN J. CANTWELL[2]

[1] Department of Mechanical Engineering, Stanford University, Stanford, CA 94305, USA
[2]Department of Aeronautics and Astronautics, Stanford University, Stanford, CA 94305, USA

(Received 20 July 1998 and in revised form 13 August 1999)

The generation of Reynolds stress, turbulent kinetic energy and dissipation in the turbulent boundary layer simulation of Spalart (1988) is studied using the invariants of the velocity gradient tensor. This technique enables the study of the whole range of scales in the flow using a single unified approach. In addition, it also provides a rational basis for relating the flow structure in physical space to an appropriate statistical measure in the space of invariants. The general characteristics of the turbulent motion are analysed using a combination of computer-based visualization of flow variables together with joint probability distributions of the invariants. The quantities studied are of direct interest in the development of turbulence models. The cubic discriminant of the velocity gradient tensor provides a useful marker for distinguishing regions of active and passive turbulence. It is found that the strongest Reynolds-stress and turbulent-kinetic-energy generating events occur where the discriminant has a rapid change of sign. Finally, the time evolution of the invariants is studied by computing along particle paths in a Lagrangian frame of reference. It is found that the invariants tend to evolve toward two distinct asymptotes in the plane of invariants. Several simplified models for the evolution of the velocity gradient tensor are described. These models compare well with several of the important features observed in the Lagrangian computation. The picture of the turbulent boundary layer which emerges is consistent with the ideas of Townsend (1956) and with the physical picture of turbulent structure set forth by Theodorsen (1955).

1. Introduction

A defining characteristic of turbulent flows is the presence of eddies over a wide range of length scales. At the low-wavenumber end of the spectrum are large, energy-containing motions and at the high-wavenumber end are the small, dissipating eddies. This paper is concerned with the behaviour of both of these motions by means of a single approach where the eigenvalues and the invariants (Q and R) of the velocity gradient tensor ($\partial U_i/\partial x_j$) are used to analyse the local motion both at an instant and over a statistical ensemble. The concepts and ideas behind this method have been amply described in the published literature. The following is only a brief summary of those concepts and the reader is referred to Chong, Perry & Cantwell (1990) for a complete treatment.

Excluded from this analysis are singular cases like vortex sheets as well as degenerate situations where the local flow pattern is determined by higher-order terms in a Taylor

† Present address: Applied Materials Inc., 3050 Bowers Avenue., M/S 0119, Santa Clara, CA 95054, USA.

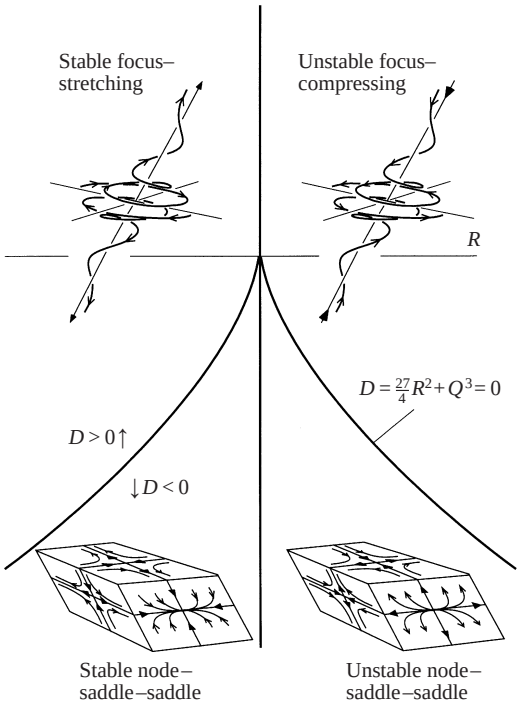

FIGURE 1. Summary of three-dimensional, incompressible flow patterns (from Soria *et al.* 1994).

series expansion of the velocity field. Under this assumption, the pattern of three-dimensional streamlines in the immediate vicinity of an observer moving with any point in the flow field is determined by the nature of the eigenvalues of the velocity gradient tensor ($A_{ij} = \partial U_i/\partial x_j$) evaluated at the point. Such eigenvalues are the roots of the characteristic equation of A_{ij} which can be written as

$$\lambda^3 + P\lambda^2 + Q\lambda + R = 0, \tag{1.1}$$

where P, Q and R are the invariants of the velocity gradient tensor. These invariants are

$$P = -A_{ii}, \tag{1.2a}$$

$$Q = \tfrac{1}{2}P^2 - \tfrac{1}{2}A_{ik}A_{ki}, \tag{1.2b}$$

$$R = -\tfrac{1}{3}P^3 + PQ - \tfrac{1}{3}A_{ik}A_{kn}A_{ni}. \tag{1.2c}$$

For incompressible flows P is identically zero leaving Q and R as the only invariants that must be considered for the classification of local flow patterns. The nature of the roots of equation (1.1) is determined by the sign of the cubic discriminant of A_{ij} which is given by the expression

$$D = \tfrac{27}{4}R^2 + Q^3. \tag{1.3}$$

If the discriminant is positive, equation (1.1) admits two complex and one real root. In this case, vorticity dominates the rate of strain, the local streamlines swirl about the point and the flow pattern is called a focus. If D is negative, all three roots

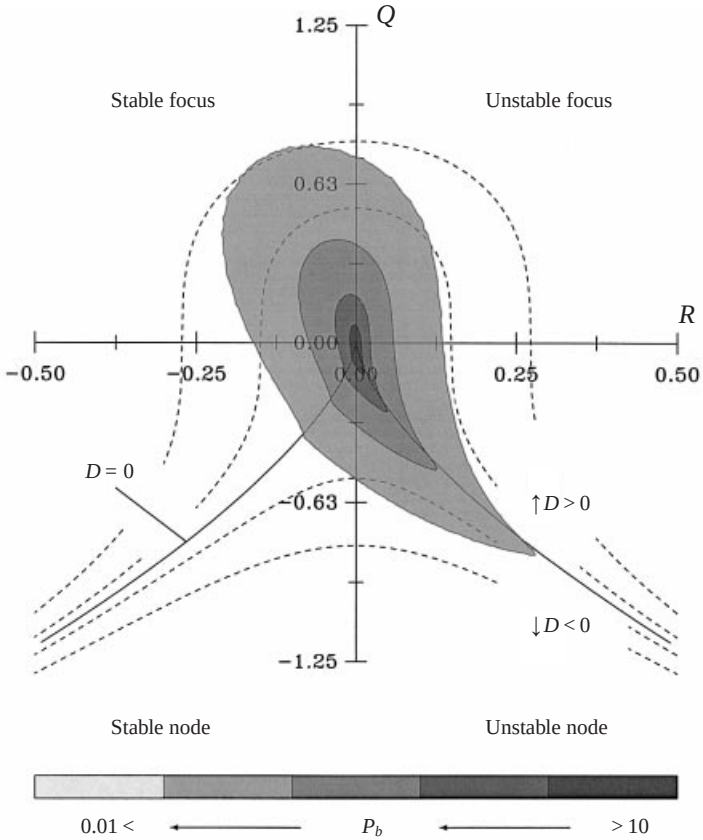

FIGURE 2. Joint probability distribution of the Q and R invariants of the velocity gradient tensor at $Re_\theta = 670$. Data taken from the entire boundary layer (from Chacin, Cantwell & Kline 1996).

of the characteristic equation are real, the rate of strain dominates the vorticity and the flow pattern is that found near a stagnation point. This type of flow geometry is called a node–saddle–saddle. All the possible types of motion that can occur in a three-dimensional incompressible flow field are summarized in figure 1 from Soria *et al.* (1994).

The occurrence and distribution of these local flow patterns in various turbulent flows have also been studied and documented in the literature. In these flows (time-developing incompressible mixing layers in Soria *et al.* 1994; turbulent channel flow by Blackburn, Mansour & Cantwell 1996; turbulent boundary layer by Chacin, Cantwell & Kline 1996; and recently in a separated boundary layer by Chong *et al.* 1998) the invariants Q and R were computed at every point in the flow and cross-plotted in the (Q, R)-plane to create a joint probability distribution for the invariants. It was found that all the possible flow patterns occurred but with different probabilities. Furthermore, it was also found that the distribution of these four classes of local geometries was remarkably similar in all flows. These PDFs exhibit a distinctive tear-drop shape like that shown in figure 2 computed from the Spalart (1988) simulation and which includes data for the entire turbulent boundary layer. These data were obtained from a sample of 786 million grid points gathered over 500 computational realizations of the flow. This accounts for the smoothness of the PDF. Since the velocity gradients associated with the fine-scale motion are larger than those for the

mean flow by a factor of $Re^{1/2}$, the tear-drop shape of the distribution shown in figure 2 is primarily a feature of these small eddies. For this reason, it has been argued that the observed repeatability of this shape is a universal characteristic of the small-scale motions of turbulence. These same ideas have also been used to study the larger, energy-containing motions (see Blackburn *et al.* 1996 and Chacin *et al.* 1996) in the context of turbulence structure.

In this paper, the invariants of the velocity gradient tensor are used to study the physical and statistical relationship between these two ends of the spectrum of length scales and to look at some details of the mechanisms of turbulence production and dissipation.

2. Turbulence generation and structure

While joint probability distributions of Q and R like that shown in figure 2 are useful in studying some of the statistical and geometrical properties associated with specific flow patterns, they say nothing about whether points in the flow with a common topological classification are gathered together in physical space forming coherent eddies. Over the years, numerous techniques have been developed to study the organized motions of turbulent flows. They range from classic experimental methods using flow markers like hydrogen bubbles (see for example Schwartz & Smith 1983 and Kline *et al.* 1967) to frame-of-reference based procedures utilizing particle image velocimetry (Meinhart & Adrian 1995).

Here, the discriminant of the velocity gradient tensor is used to address this issue. This scalar (see equation (1.3)) combines the information contained in the Q and R invariants into a single scalar quantity which is a measure of the local tendency for the velocity field to roll or stretch fluid elements. From figure 1 it can be seen that

$$D \begin{cases} > 0 & \text{two complex and one real root (i.e. focus topology)} \\ \leqslant 0 & \text{three real roots (i.e. node-saddle-saddle topology).} \end{cases} \tag{2.1}$$

The approach used by Blackburn *et al.* (1996), Chacin *et al.* (1996) and Chong *et al.* (1998) is to use D as a marker of coherent motions in the flow. An example of the structures revealed in this manner is shown in figure 3 for the flat-plate turbulent boundary layer flow at $Re_\theta = 670$. This figure (showing a top view of the flow) shows elongated, streamwise-oriented structures that sometimes arch spanwise to form horse-shoe-shaped eddies. More commonly though, as was also noticed by Robinson (1990), Blackburn *et al.* (1996), Brooke & Hanratty (1993) and many others, the structures are seen to form bunches of intertwined helical tubes oriented predominantly in the streamwise direction.

As a practical matter, the isosurface used for the construction of figure 3 was $D = 0.05$ instead of $D = 0$. This was done in order to avoid interpolation errors by the flow visualization software. The maximum value of the discriminant in the flow realization shown in the figure was of the order of 700. The repeatability of the events presented in this figure was confirmed with the use of a computer animation of the flow comprising over 500 time steps which lasted, in time normalized by wall variables (tu_τ^2/ν), just over 104 non-dimensional time units or about 2 flow-through times. The events shown in this figure are typical of what was observed in the animation.

Recently Jeong & Hussain (1995) introduced a procedure for the study of turbulence structure based on the symmetric tensor $B_{ij} = S_{ik}S_{kj} + W_{ik}W_{kj}$ (where $\boldsymbol{S}$ and $\boldsymbol{W}$ are the rate-of-strain and rate-of-rotation tensors). Because of the symmetry of $\boldsymbol{B}$, all three of its eigenvalues are real and can be ordered as $\lambda_1 > \lambda_2 > \lambda_3$. According to this

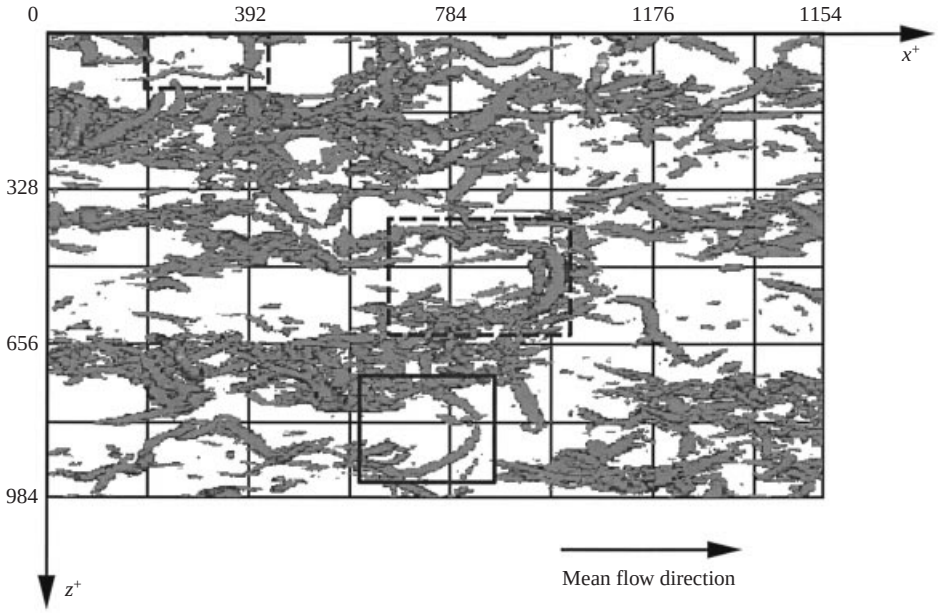

FIGURE 3. Top view of the computational domain showing regions of positive discriminant. From Chacin *et al.* (1996).

approach, a vortex structure is a connected region of the flow where $\lambda_2 < 0$. Both this technique and the discriminant-based method were used by Loulou (1996) to study a DNS of pipe flow and gave visually similar results. Because of this, an attempt was made to relate the two methods by expressing the invariants of $\boldsymbol{B}$ in terms of the invariants of the velocity gradient tensor $\boldsymbol{A}$. The details of this analysis can be found in Chacin & Cantwell (1997). It was found that such a relationship cannot be established. That is, the invariants of $\boldsymbol{B}$ depend not only on the invariants of $\boldsymbol{A}$ but also on the individual components of $\boldsymbol{A}$ as follows:

$$P_B = 2Q, \tag{2.2a}$$

$$Q_B = \tfrac{1}{2}\left\{3Q^2 - \tfrac{1}{2}\left(A_{ip}A_{pk}\right)\left(A_{ir}A_{rk}\right\}\right), \tag{2.2b}$$

$$R_B = \tfrac{1}{4}\left\{2Q^3 - R^2 - Q\left(A_{ip}A_{pk}\right)\left(A_{ir}A_{rk}\right) + R\left(A_{ik}\right)\left(A_{ip}A_{pk}\right)\right\}. \tag{2.2c}$$

An implication of equations (2.2*b*, *c*) is that an affine transformation used to generate a new $\boldsymbol{A}$ will leave its invariants unchanged but will generate a new $\boldsymbol{B}$ with a new set of invariants. This fact together with the symmetrization used to define $\boldsymbol{B}$ makes it difficult to relate the invariants of this tensor to the velocity vector field of the flow, which is the basis for most structural observations in the literature including Kline *et al.* (1967), Robinson (1990), Bernard, Thomas & Handler (1993), Brooke & Hanratty (1993) and many others. Empirical comparisons using the DNS data suggest that the procedure of Jeong & Hussain (1995) is essentially equivalent to marking points where $Q > 0$ although this cannot be precisely established.

A close-up view of one of the eddies identified using the discriminant (enclosed in the square in figure 3) is shown in figure 4. This view is strikingly reminiscent of the near-wall structure dominated by attached vortices proposed by Theodorsen (1955), Townsend (1956), Kline *et al.* (1967), Head & Bandyopadhyay (1978), Robinson (1990) and others and serves to emphasize the physical significance of the invariants of the velocity gradient tensor and the discriminant. It also serves as a reminder that

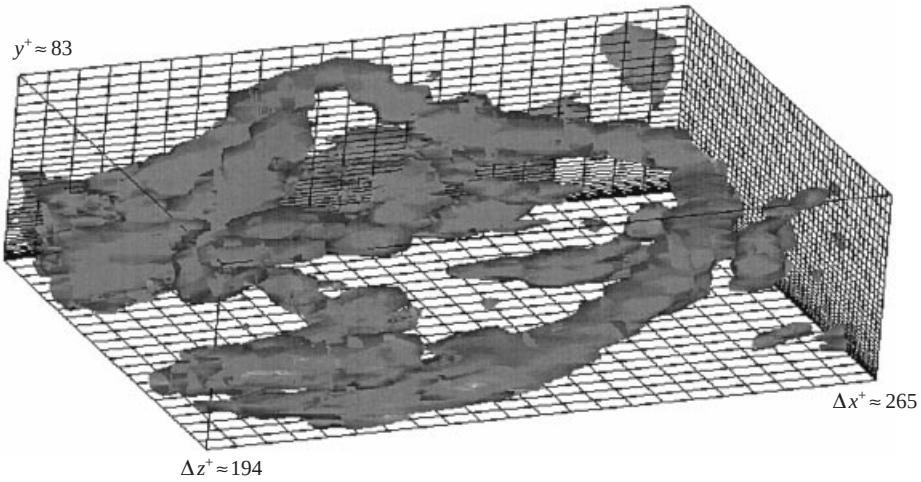

FIGURE 4. Close-up view of near-wall structure. From Chacin *et al.* (1996).

vorticity alone is not an adequate identifier of swirling flow structure. The eddies shown in these figures have streamwise dimensions of the order of several hundred wall units (length normalized using the friction velocity u_τ and the kinematic viscosity ν) and are thus important contributors to the large-scale motion. It could then be expected that they would play an important role in the production of turbulence within the flow. One of the interesting features of this figure is the presence of large blank regions. These blank spaces correspond to $D < 0$ and it is of interest to ask whether there is any significant turbulent activity there.

Regardless of whether or not the discriminant of the velocity gradient tensor is useful for the visualization of flow structure, it is of greater interest to study the relationship between these eddies defined by the invariants of A_{ij} and regions of the flow that are active in terms of Reynolds shear stress generation ($-\overline{u'v'}$). For the case of this flow (with homogeneous spanwise coordinate and slow streamwise evolution), it is possible to establish a direct connection between the second invariant Q and the $\overline{v'^2}$ component of the Reynolds stress tensor. Taking the time average of equation (1.2) and setting all the gradients in the x- and z-directions to zero, gives

$$\overline{Q} \approx -\frac{1}{2}\frac{\partial^2 \overline{v'^2}}{\partial y^2}. \tag{2.3}$$

This equation begins to establish a link between these descriptors of flow geometry (Q, R and D) and the dynamics of turbulence generation. A broader view of this connection between invariants and Reynolds stresses is shown in figure 5. This figure shows the same view of the flow field shown in figure 3 with added contours of constant Reynolds shear stress in magenta and yellow. These contours show events that are significantly stronger than the time-averaged values of Reynolds shear stress. There is a clear spatial association between the $D = 0$ surfaces and these Reynolds-stress-generating events. The statistical significance of this statement will be discussed shortly.

Bernard *et al.* (1993) examined a turbulent channel flow in detail and found that, although there is a clear association between flow structure and Reynolds stress, the majority of the stress was generated in a relatively small number of isolated events. This behaviour is also observed in figure 5. This mechanism is explored further in

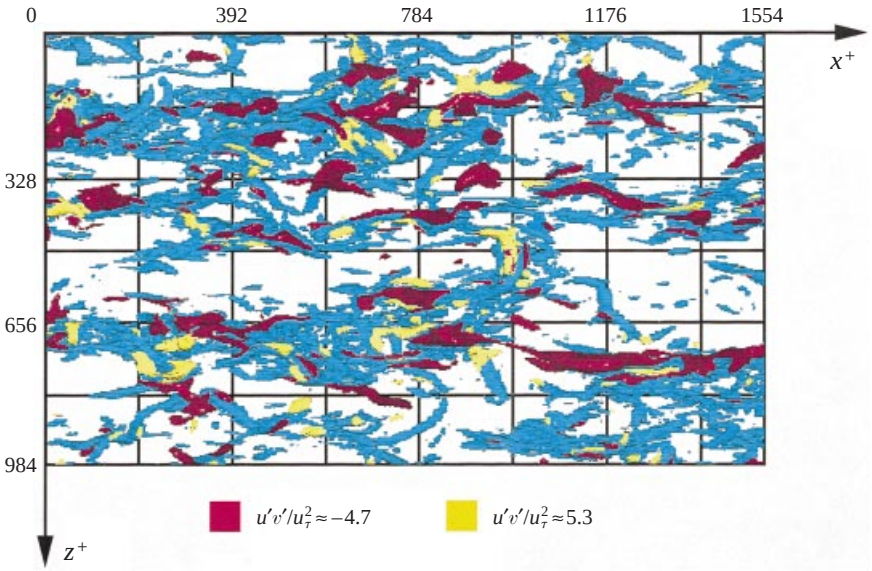

FIGURE 5. Top view of the computational domain showing regions of positive discriminant and their spatial association with Reynolds stress events ($u'v'$).

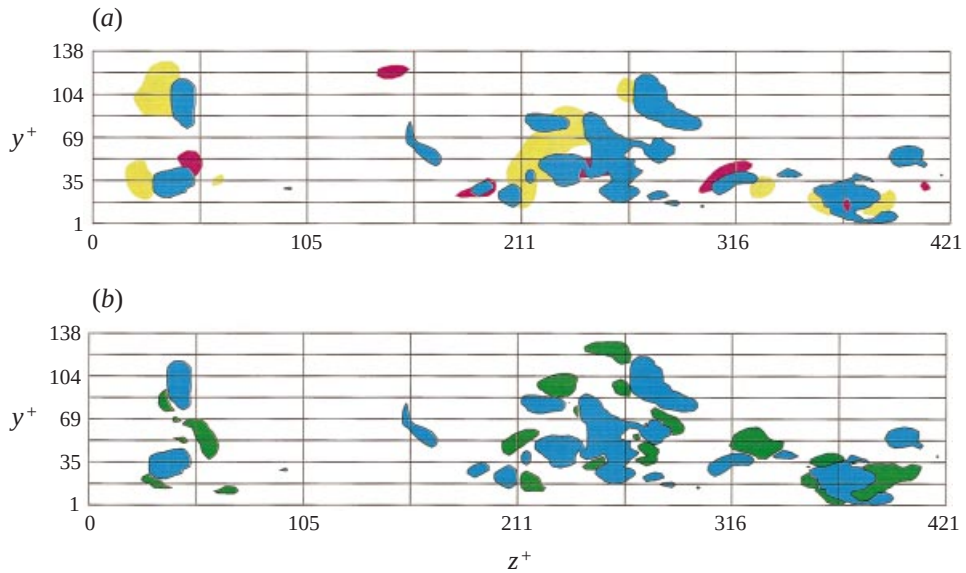

FIGURE 6. Spanwise cut of the computational domain. (*a*) Regions of positive discriminant, in blue, and their spatial association with Reynolds stress events $u'v'$, in magenta and yellow (the contour levels shown are the same ones used in figure 5). (*b*) Same view showing regions of positive discriminant, in blue, and regions of extreme negative discriminant in green.

figure 6(*a*, *b*). Figure 6(*a*) is a spanwise cut across a section of the computational domain with regions of positive discriminant as well as contours of constant $-u'v'$ depicted in the same way as in figure 5. This figure emphasizes the presence of active motions as proposed by Townsend (1956), which seem to take place in regions that are adjacent to the flow structures marked by the discriminant of the velocity gradi-

ent tensor. This particular view is also reminiscent of the observations on the origin of vortices in near-wall turbulence in channel flow by Brooke & Hanratty (1993). Another interesting characteristic of these motions is highlighted in figure 6(*b*) which shows the same view of the flow as that shown in figure 6(*a*). In this view however, the blue areas enclose the points in the flow where the discriminant is positive and bigger than 0.05 (the largest positive D values are on the order of 700 to 1500 depending on the realization) whereas the green zones are regions where D is negative and smaller than -0.1 (the most negative values of D are on the order of -200 to -300). Therefore, these coloured spots surround the local extrema of the discriminant of the velocity gradient tensor. By comparing these two views, it can be seen that the local extrema of the discriminant (both maximum and minimum) seem to take place in close spatial proximity to each other and it is in these regions of high spatial gradient of the discriminant that the Reynolds-stress-generating events seem to occur. Thus the blank regions noted earlier are not entirely free of activity but the activity is confined to the neighbourhood of the $D = 0$ surfaces. The remaining blank regions in figure 6(a, b) are truly passive as far as Reynolds stress generation is concerned. As mentioned earlier, the repeatability of all these observations was ascertained with a computer-based animation of the flow that comprised over two flow-through times.

This characteristic of the active motions can be further analysed with the help of the (Q, R)-plane shown in figure 2. The two invariants (Q and R) are of course continuous functions and must therefore vary smoothly in space. Indicated by the dotted lines in that figure are curves of constant discriminant value. As can be seen, in the lower-right and lower-left quadrants of the plane, the lines of constant D asymptote toward the $D = 0$ curve and are closely grouped together. In these regions, a small change in either or both Q and R will produce a much larger change in the value of D than in any other part of the (Q, R)-plane. However, the joint probability distributions of the invariants shown in figure 2 shows that there are significantly more data points in the lower-right quadrant than in the lower-left side of the plane. It is in this quadrant then, and in the flow patterns associated with it (unstable focus–compression and unstable node–saddle–saddle), that the strongest Reynolds shear stress generating events are most likely to occur.

In order to verify this argument, and to determine if these strong, instantaneous bursting events are statistically important, the time-averaged value of this component of the Reynolds stress tensor associated with each flow topology was computed. The result is shown in figure 7. For this figure, the values of the two invariants (Q and R) as well as the instantaneous value of $u'v'$ were computed at every point in the flow for over 700 time realizations (1.1×10^9 data points). The results were averaged in time and plotted in the (Q, R)-plane. The values of the contour levels shown have been normalized by u_τ^2. Even though all flow patterns contribute to the mean negative value of $u'v'$, the peculiar shape shown in figure 7 confirms that the strongest events are located toward the tail of the Q, R distribution with the highest value corresponding to unstable focus–compression and unstable node–saddle–saddle motions. By keeping track of the sign of the velocity fluctuations during the time-averaging process, it was also possible to classify the two peaks shown in the figure using the quadrant decomposition technique of Wallace, Eckelmann & Brodkey (1972). As indicated in figure 7, it was observed that the strong $u'v'$ motions with a node–saddle–saddle classification were primarily sweeps ($+u', -v'$). Those above the $D = 0$ curve, with flow pattern of the type unstable-focus compression were mostly ejections ($-u', +v'$).

Figure 7 shows the result for the entire boundary layer from the wall to the free stream and, therefore, obscures the details of what happens at different distances

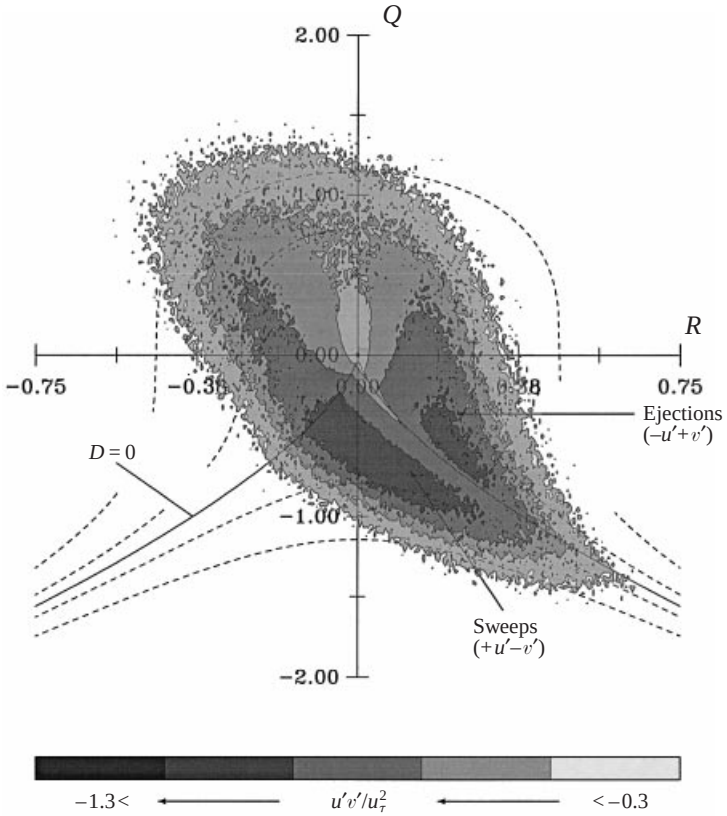

FIGURE 7. Time-averaged Reynolds-shear-stress ($u'v'$) generating events associated with the four incompressible flow patterns. Data taken from the entire boundary layer.

from the wall. This issue is addressed in figure 8(*a–d*). As indicated in the figure, the boundary layer was divided into four regions (viscous layer, buffer region, log layer and the wake) and the same calculation for $-\overline{u'v'}$ was repeated in each separate zone. In the viscous sublayer (figure 8*a*), the turbulence level is predictably low. Nonetheless, the unstable node–saddle–saddle topology is the only kind of flow pattern that contributes significantly to the Reynolds shear stress. These events are predominantly near-wall sweeps ($+u', -v'$) or high-speed fluid rushing toward the wall. Moving upward from the wall, from the buffer region to the outer layer (figure 8*b–d*), the profiles are similar to that shown in figure 7. The only noticeable effect of the diminishing role of viscosity is the change in the scales, with the largest range of contours occurring in the buffer region (where the production term $-\overline{u'v'}\partial\overline{U}/\partial y$ and the turbulence intensities also peak). For every one of these regions (buffer, log layer and wake) the strongest Reynolds stress events were associated with motions of unstable node–saddle–saddle and unstable focus–compression topology and these events are located, in physical space, in regions where the discriminant changes sign rapidly. These are regions where swirling flow occurs in close physical proximity to strongly rate-of-strain-dominated flow.

Given the association found between the large-scale motions (visualized using the discriminant) and the Reynolds shear stresses, it seems reasonable to explore whether there exists a similar kind of correlation between these structures and additional components of the Reynolds stress tensor. Of particular interest is the trace of this

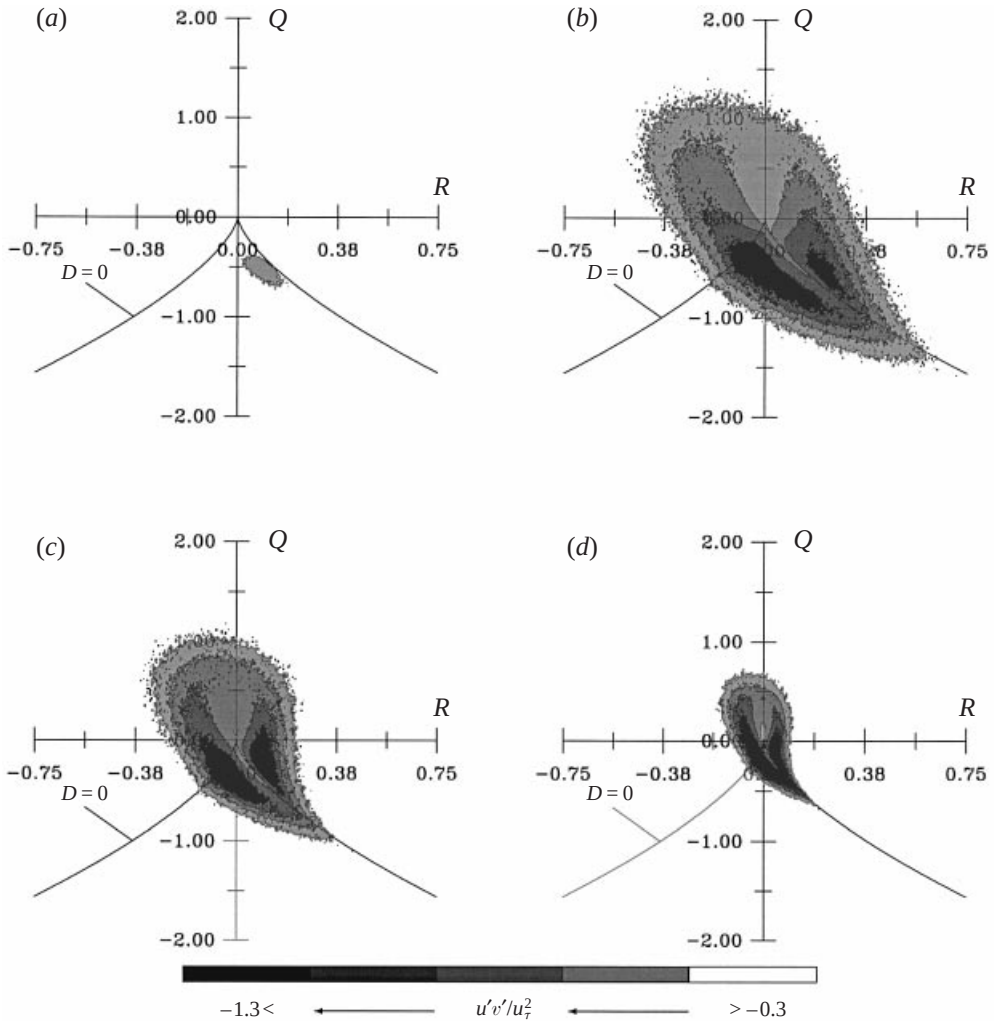

FIGURE 8. Time-averaged Reynolds-shear-stress ($u'v'$) generating events associated with the four incompressible flow patterns as a function of distance from the wall. (*a*) $y^+ < 5.0$, (*b*) $5.0 < y^+ < 41$, (*c*) $41 < y^+ < 107$, (*d*) $y^+ > 107$.

tensor, the turbulent kinetic energy. Figure 9 shows, in light grey, regions of positive discriminant and superposed (in darker grey) are isocontours of instantaneous values of the turbulent kinetic energy, TKE ($k = \overline{u_i' u_i'}/2$). The contour level plotted is $u_i' u_i'/2u_\tau^2 \approx 14.8$. The peak, time-averaged value of k for this flow is approximately 4.3. As can be seen, these regions are mostly elongated and oriented in the streamwise direction and, as was the case for the Reynolds shear stress, there is a visible spatial association between them and the $D > 0$ eddies. This can be seen more clearly by observing that the areas of the figure where there are no visible, neighbouring structures of focus-type topology are also completely devoid of motions with high values of k. So the blank regions referred to earlier seem to be truly passive in the sense used by Townsend (1956).

As was done for the shear stress component of the Reynolds stresses tensor, the motions associated with the events shown in figure 9 were catalogued using the (Q, R)-plane. Figure 10 shows the time-averaged data for the entire boundary layer. The

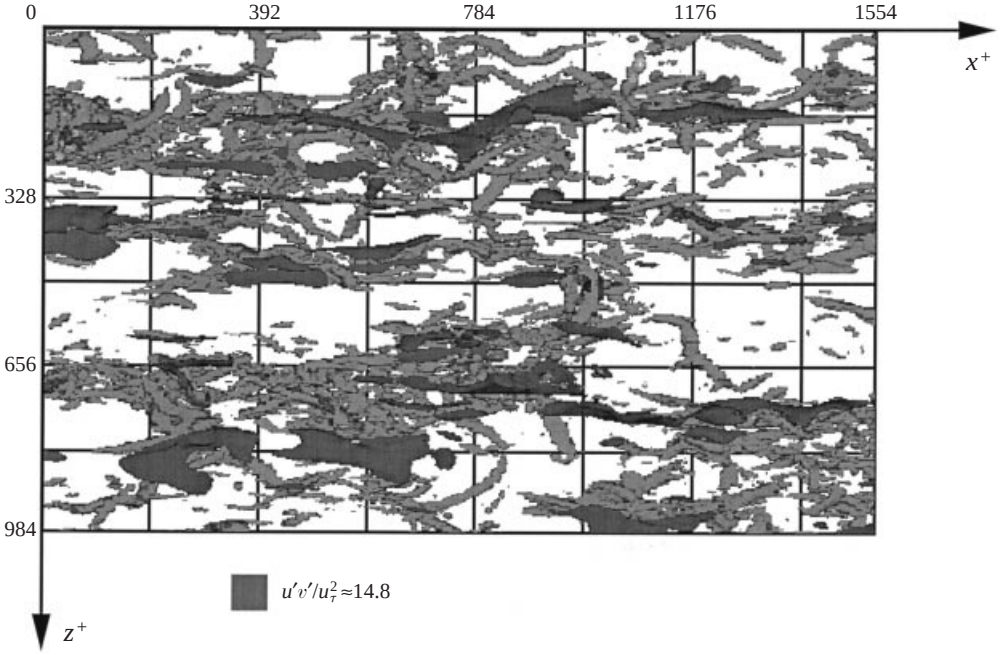

FIGURE 9. Top view of the computational domain showing regions of positive discriminant and their spatial association with regions of high, instantaneous turbulent kinetic energy events ($u_i'u_i'$).

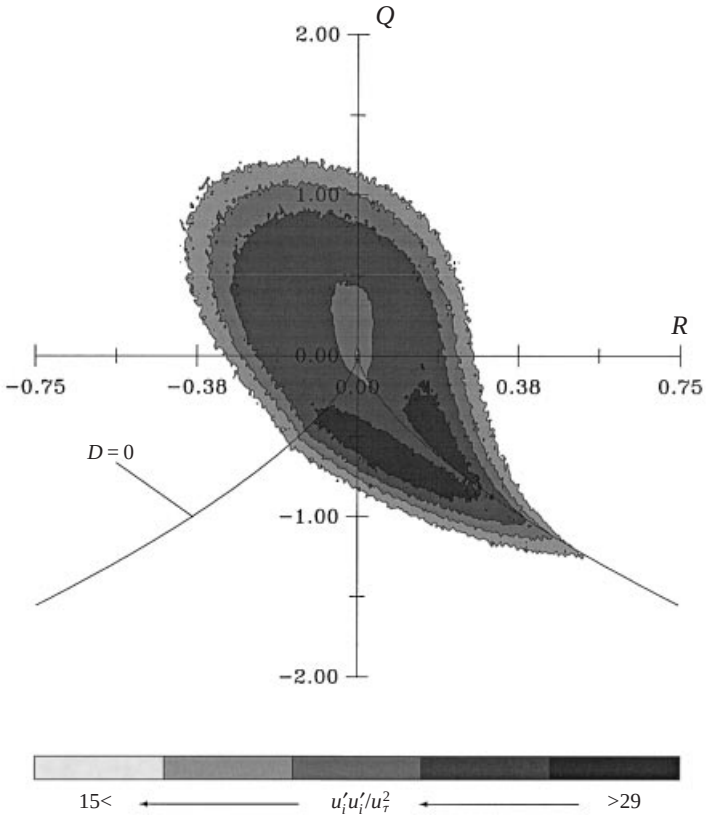

FIGURE 10. Time-averaged TKE generating events associated with the four incompressible flow patterns. Data taken from the entire boundary layer.

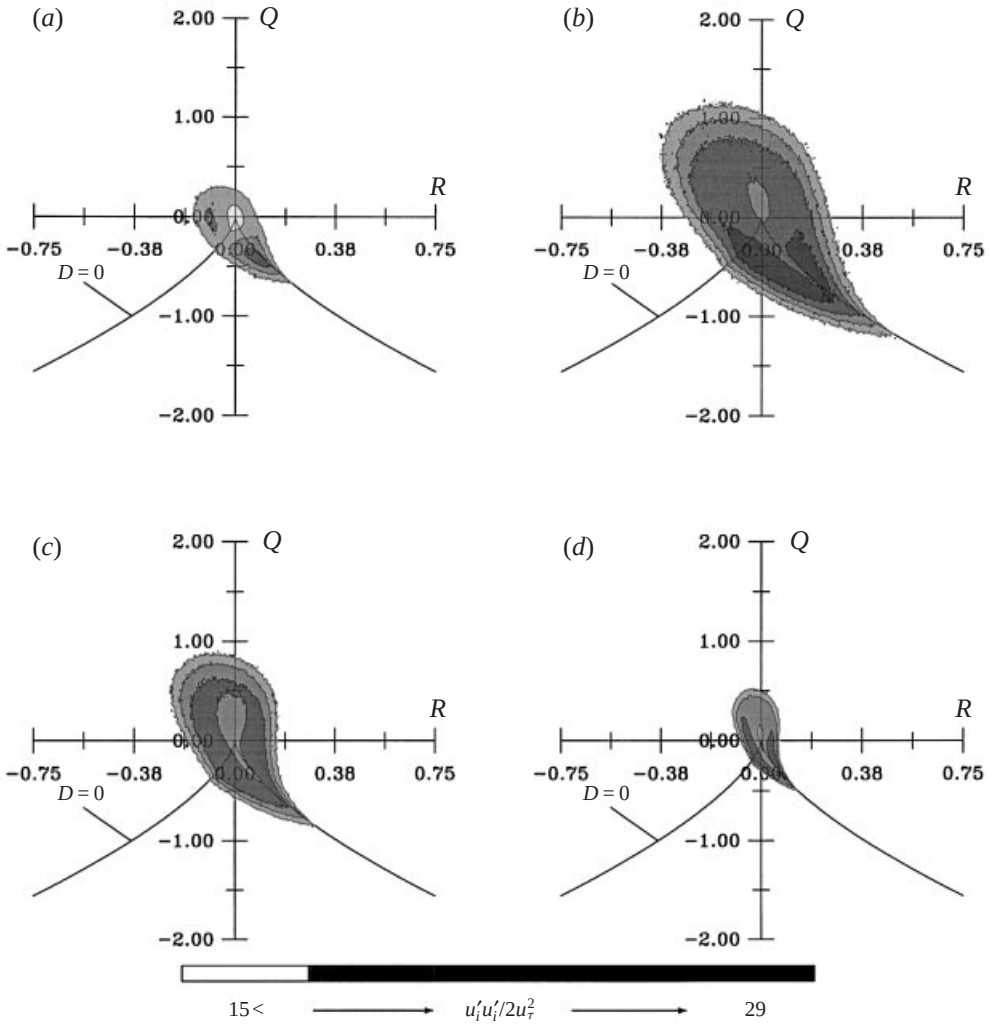

FIGURE 11. Time-averaged TKE-generating events associated with the four incompressible flow patterns as a function of distance from the wall. (*a*) $y^+ < 5.0$, (*b*) $5.0 < y^+ < 41$, (*c*) $41 < y^+ < 107$, (*d*) $y^+ > 107$.

shape of the figure is rather similar to that for the $-\overline{u'v'}$ with the strongest motions, in terms of turbulent kinetic energy, being again of the type unstable focus–compression and unstable node–saddle–saddle. It is interesting to notice that, moving away from the origin toward larger values of the invariants (positive or negative), the intensity of the turbulent kinetic energy first increases but then decreases toward the outer contours of the probability distribution.

The variation of this mechanism of TKE generation with distance from the wall is shown in figure 11(*a–d*). Data were once again gathered at four different y^+ regions within the turbulent boundary layer corresponding to the viscous sublayer, buffer region, logarithmic layer and the wake region. Below $y^+ \approx 41$, where most of the production of turbulence takes place, the tendency shown in figure 10 holds and the most intense motions are located in the lower-right quadrant of the plane just above and below the $D = 0$ curve. Recall from figure 2 that the vast majority of data points

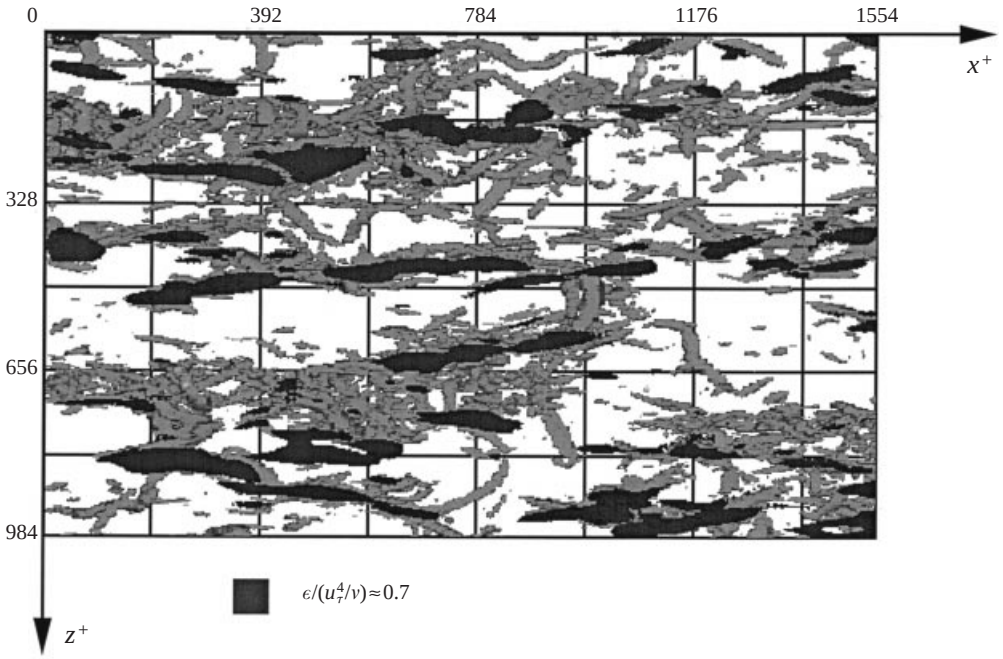

FIGURE 12. Top view of the computational domain showing regions of positive discriminant and their spatial association with regions of high, instantaneous turbulent kinetic energy dissipation events ($2\nu\overline{s'_{ij}s'_{ij}}$).

lie near the origin in the (Q, R)-plane. The contours shown in figure 11(*a–d*) indicate that the generation of turbulence occurs in a small number of intense, isolated events that are characterized by a strong spatial gradient of the discriminant.

In statistically stationary turbulence, the production of turbulent kinetic energy is balanced by the dissipation. Even though this dissipation is accomplished by the small scales of the flow, its behaviour is governed by the large eddies and the rate at which they transfer energy through the cascade. This quantity has additional practical significance in that many turbulence models (and subgrid-scale models for large eddy simulation) owe their usefulness, at least in part, to the fact that they can account for the dissipation with reasonable accuracy. Figure 12 is a similar view to that shown in figure 9 but, for this figure, an isocontour of $\epsilon/(u_\tau^4/\nu) \approx 7.5$ was superposed (in dark grey) where ϵ is the dissipation of turbulent kinetic energy

$$\epsilon = \nu \frac{\partial u_i'}{\partial x_j}\left(\frac{\partial u_i'}{\partial x_j} + \frac{\partial u_j'}{\partial x_i}\right). \tag{2.4}$$

Compared to the time-averaged profiles, the dissipation level used for these iso-contours is about 8 times the peak mean value. Two observations are apparent. First, there is the same kind of spatial proximity between dissipating events and regions of $D > 0$. Within the focal regions themselves, the dissipation is lower, which seems to indicate that they will have a relatively long life. Second, comparing figures 9 and 12, it can be seen that the regions of high dissipation are somewhat similar to those of high k. Mean flow energy is converted into turbulent kinetic energy by the large eddies and, as such energy grows in a particular region, the dissipation grows with it.

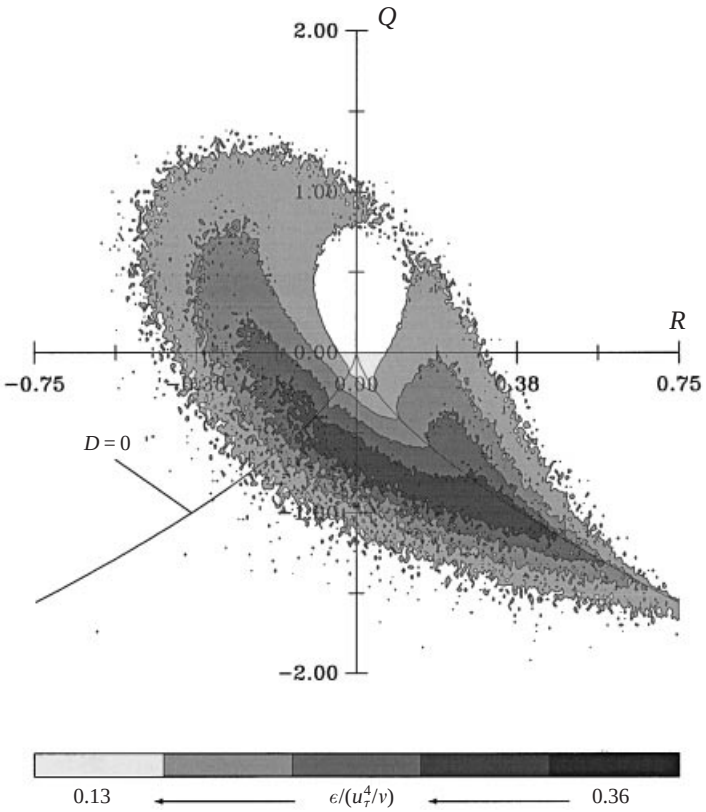

FIGURE 13. Time-averaged dissipative events associated with the four incompressible flow patterns. Data taken from the entire boundary layer.

In spite of the similarities between figures 9 and 12, there are however differences that are revealed by the use of time-averaging in the (Q, R)-plane shown in figure 13. There are two readily noticeable aspects. First, most of the dissipation occurs below the $D = 0$ curve in motions of type node-saddle-saddle (both stable and unstable). Second, motions closely aligned with the positive side of the Q-axis seem to have very low values of dissipation. For these motions, the velocity gradient tensor has two purely complex eigenvalues with no out-of-plane strain, a motion akin to a two-dimensional vortex. Furthermore, by splitting the velocity gradient tensor into its symmetric and antisymmetric parts

$$A_{ij} = S_{ij} + W_{ij} \tag{2.5}$$

it can be shown in a straightforward manner that the second invariant Q can be written as

$$Q = \tfrac{1}{2}\left(W_{ij}W_{ij} - S_{ij}S_{ij}\right); \tag{2.6}$$

hence, the structures near the positive vertical axis of the (Q, R)-plane are ones in which the vorticity dominates the motion of the fluid.

Miyake & Tsujimoto (1996) studied conditionally sampled, streamwise vortex tubes in a numerically simulated channel flow. The authors kept careful track of the magnitude of all the terms that appear on the right-hand side of the evolution equation for the streamwise vorticity component (w_x), in particular the vortex stretching and

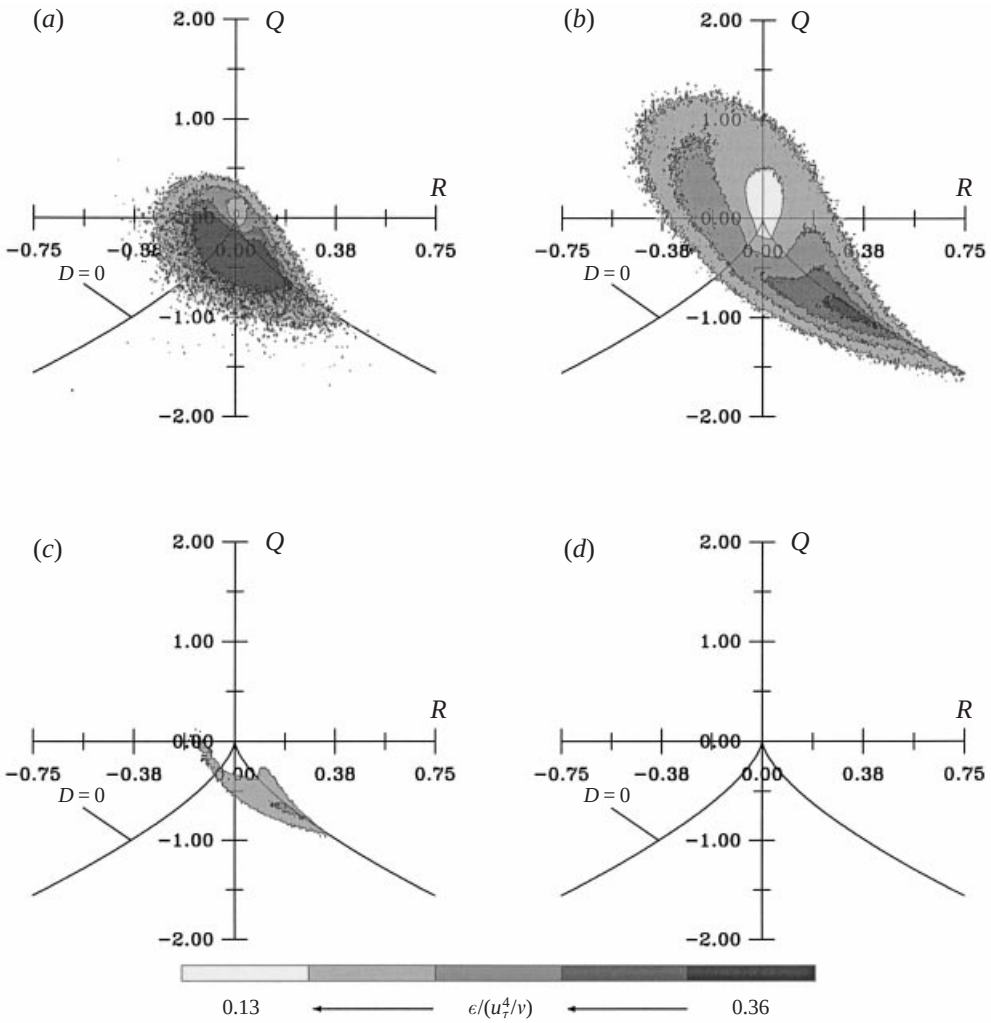

FIGURE 14. Time-averaged dissipative events associated with the four incompressible flow patterns as a function of distance from the wall. (*a*) $y^+ < 5.0$, (*b*) $5.0 < y^+ < 41$, (*c*) $41 < y^+ < 107$, (*d*) $y^+ > 107$.

viscous dissipation terms. They found that streamwise vortex tubes continue to exist long after the production of w_x has ceased. The peculiar shape shown in figure 13 is consistent with that observation since it indicates that these vortex tubes are motions undergoing little energy dissipation and comparatively low strain. It also suggests that flow structures like those shown in figure 3 will have a long life. This was confirmed using the computer animation of the flow mentioned earlier in which some of these eddies were seen to convect, almost without change, for at least $\Delta t^+ = 40$ ($t^+ = tu_\tau^2/\nu$).

Figure 14(*a–d*) shows the time-averaged dissipation contours taken from the four different regions of the boundary layer. The tendency observed for the dissipation of energy to occur mostly in motions of type node–saddle–saddle is particularly noticeable away from the wall (figure 14*b*, *c*). The absence of significant energy dissipation away from the wall is apparent in figure 14(*d*) as would be expected.

A comprehensive study of the kinematics of turbulence was carried out by Robinson

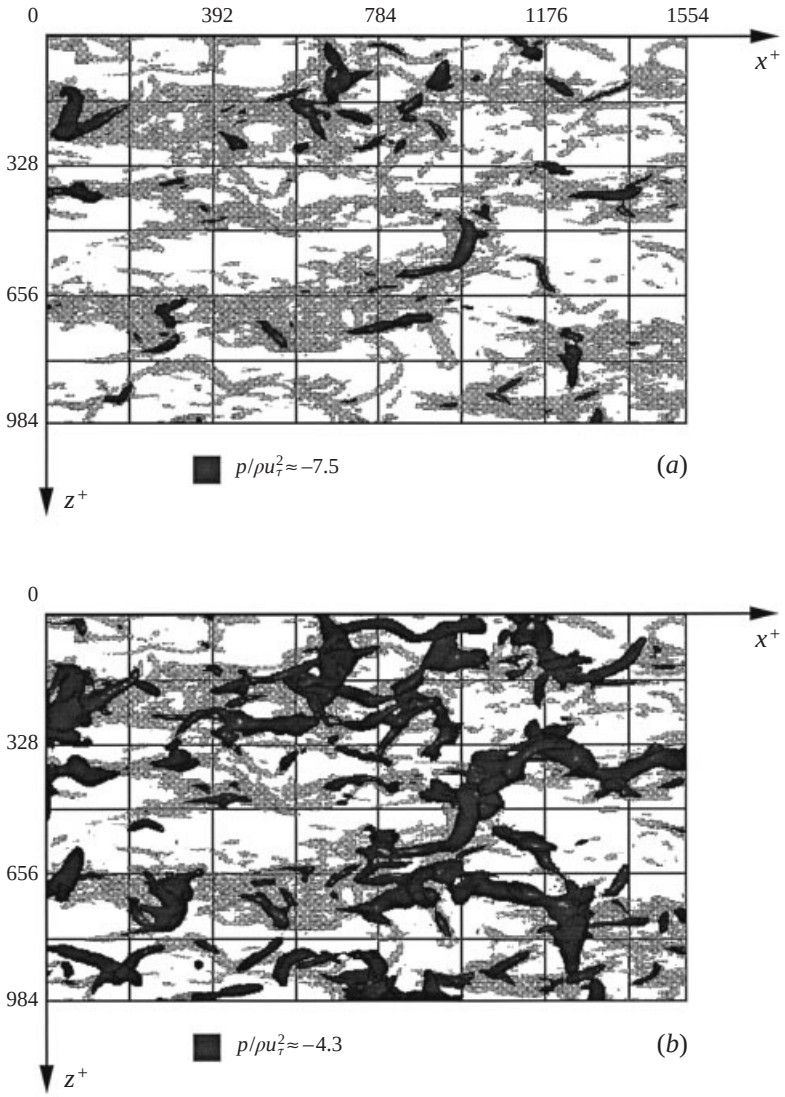

FIGURE 15. Top view of the computational domain showing regions of positive discriminant (light grey) and their spatial association with the instantaneous pressure field (dark grey).

(1990) on the same numerical simulation data presented here. In that work, the author prepared a taxonomy of all the different types of coherent events that have been observed in turbulent flows. He points out the importance of vortical motions and how they could be used to connect various other types of flow structures and he uses the pressure field as a means of identifying these vortical motions. The rationale is that, for a two-dimensional vortex with near-circular streamlines the pressure must reach a minimum at the vortex centre. In the absence of such near-circular streamlines however, the extrema in the pressure field need not occur.

Figure 15(a, b) shows the same view of the computational domain used in figure 3 with surfaces of constant pressure superimposed onto the structures visualized using the discriminant. The free stream pressure is zero in the computation. These latter contours were made transparent to facilitate the comparison since pressure minima

commonly lie inside the surface $D = 0$. Two pressure thresholds were used at $p/(\rho u_\tau^2) \approx -7.5$ (figure 15*a*) and $p/(\rho u_\tau^2) \approx -4.3$ (figure 15*b*). This last level encloses the regions of the flow with the lowest instantaneous pressure and is the same one used by Robinson (1990) in his study. As can be seen in the figure, there is a general correspondence between the two fields. In particular, pressure minima generally occur where the discriminant is positive. The association however is not universal.

This issue can be further explored by examining some of the properties of the pressure field which is governed by Poisson's equation. Using the definition of the second invariant Q (equation (1.2)) this equation can be written as

$$\nabla^2 p = 2Q. \tag{2.7}$$

For any three-dimensional function, a necessary condition for the existence of a local minimum is

$$\nabla^2 p > 0, \tag{2.8}$$

so local pressure minima and regions of positive discriminant can only coincide in areas where $Q > 0$. As was shown in the joint probability distributions of Q and R in figure 2, there is a significant number of flow structures where $D > 0$ and $Q < 0$. These regions cannot be seen using isocontours of low pressure and, as indicated by figure 7, these areas are important in Reynolds shear stress generation.

In addition, the use of the pressure field presents the additional complication that a threshold level must be chosen. For a relatively simple flow, with no mean pressure gradient like this one, this selection is not unduly cumbersome. For a more complex flow with pressure gradients it may not be possible to do so without a certain degree of arbitrariness. This problem is avoided by the use of the velocity gradient tensor invariants, and the discriminant, since the threshold value used ($D = 0$) is unmistakably determined by the boundary between complex and real roots for the characteristic equation (equation (1.1)). See for example Chong *et al.* (1998) where the method is applied to the separating flow computed by Na & Moin (1996).

3. Time-evolution of flow invariants

In the previous sections, the invariants of the velocity gradient tensor were used to characterize a turbulent flow by separating it into two basic types of flow structures. In one kind – focus type – the rotational part of $\partial U_i/\partial x_j$ controls the shape of the local streamlines. On the other – node–saddle–saddle type – the irrotational part of the velocity gradient is the determining factor. The picture presented there seems to indicate that additional insight into turbulent motions can be gained by studying the evolution of these flow structures as well as the interactions between them. In this section, this issue is further studied by tagging and following individual fluid particles as they convect with the flow. In doing this, it was possible to gather information about the time-evolution of the invariants Q and R (and hence the discriminant D) in a Lagrangian frame of reference.

The exact evolution equations for the invariants of the velocity gradient tensor were obtained by Cantwell (1992). The procedure for constructing these equations is briefly summarized here. Taking the gradient of the Navier–Stokes equations ($\partial/\partial x_j$) and substituting $A_{ij} = \partial U_i/\partial x_j$ into the resulting relation leads to

$$\frac{\partial A_{ij}}{\partial t} + U_k \frac{\partial A_{ij}}{\partial x_k} + A_{ik} A_{kj} = -\frac{\partial^2 p}{\partial x_i \partial x_j} + \nu \frac{\partial^2 A_{ij}}{\partial x_k \partial x_k}. \tag{3.1}$$

Taking the trace of equation (3.1) leads to Poisson's equation for the pressure field

$$A_{ik}A_{ki} = -\frac{\partial^2 p}{\partial x_i \partial x_i} = -2Q. \tag{3.2}$$

Subtracting equation (3.2) from equation (3.1) produces

$$\frac{\partial A_{ij}}{\partial t} + U_k \frac{\partial A_{ij}}{\partial x_k} + A_{ik}A_{kj} - (A_{km}A_{mk})\frac{\delta_{ij}}{3} = H_{ij}, \tag{3.3}$$

where the tensor H_{ij} is given by

$$H_{ij} = -\left(\frac{\partial^2 p}{\partial x_i \partial x_j} - \frac{\partial^2 p}{\partial x_k \partial x_k}\frac{\delta_{ij}}{3}\right) + \nu \frac{\partial^2 A_{ij}}{\partial x_k \partial x_k}. \tag{3.4}$$

The evolution equation for Q is constructed by multiplying equation (3.3) by A_{jk} and taking the trace of the resulting tensor relation. Similarly, the equation for the third invariant R is the trace of the tensor equation obtained after multiplying equation (3.3) by $A_{jk}A_{kp}$. The final evolution equations are

$$\frac{\mathrm{d}Q}{\mathrm{d}t} + 3R = -A_{ik}H_{ki}, \tag{3.5}$$

$$\frac{\mathrm{d}R}{\mathrm{d}t} - \tfrac{2}{3}Q^2 = -A_{ik}A_{kn}H_{ni}, \tag{3.6}$$

where $\mathrm{d}/\mathrm{d}t$ is the convective time-derivative operator. Relatively little is known about the behaviour of H_{ij} however. Cheng & Cantwell (1996) computed all the terms in equation (3.4) for a homogeneous, isotropic turbulent flow and found that this tensor has the tendency to behave approximately as

$$H_{ij} \sim -\kappa A_{ij}, \tag{3.7}$$

where κ is a positive constant with dimensions of $1/\text{time}$. This tendency was particularly noticeable in regions of high dissipation of turbulent kinetic energy. This is consistent with the model considered by Martin & Dopazo (1995). It was also found by Cheng & Cantwell (1996) that κ seems to decrease with increasing Reynolds number. Substituting this equation for H_{ij} in equations (3.5) and (3.6) results in

$$\frac{\mathrm{d}Q}{\mathrm{d}t} + 3R = \kappa A_{ik}A_{ki}, \tag{3.8}$$

$$\frac{\mathrm{d}R}{\mathrm{d}t} - \tfrac{2}{3}Q^2 = \kappa A_{ik}A_{kn}A_{ni}. \tag{3.9}$$

However, from equations (1.2b, c) $A_{ik}A_{ki} = -2Q$ and $A_{ik}A_{kn}A_{ni} = -3R$, therefore

$$\frac{\mathrm{d}Q}{\mathrm{d}t} = -3R - 2\kappa Q, \tag{3.10}$$

$$\frac{\mathrm{d}R}{\mathrm{d}t} = \tfrac{2}{3}Q^2 - 3\kappa R. \tag{3.11}$$

It is also possible to derive a Lagrangian evolution equation for the discriminant of the velocity gradient tensor under the same assumption of $H_{ij} \sim -\kappa A_{ij}$. From equation (1.3)

$$\frac{\mathrm{d}D}{\mathrm{d}t} = \frac{27}{2}R\frac{\mathrm{d}R}{\mathrm{d}t} + 3Q^2\frac{\mathrm{d}Q}{\mathrm{d}t}. \tag{3.12}$$

Substituting equations (3.10) and (3.11) it is obtained after some algebra that

$$\frac{\mathrm{d}D}{\mathrm{d}t} = -6\kappa D. \tag{3.13}$$

For $\kappa = 0$, the equations reduce to the restricted Euler model (Vieillefosse 1984) for which an exact solution exists (see Cantwell 1992) and which has the property that the discriminant is a materially conserved quantity. For any other positive value of κ, equation (3.13) indicates that fluid particles will have a time-averaged tendency to evolve toward $D = 0$.

Furthermore, observe that the system of ordinary differential equations given by (3.10) and (3.11) has two critical points. One of them is located at the origin of coordinates in the (Q, R)-plane ($Q = 0, R = 0$). The geometry of the solution trajectories of this system in the neighbourhood of this point can be studied using standard two-dimensional phase-space techniques. Since the critical point is located at the origin, the quadratic term in equation (3.11) may be neglected and only the linear term need be considered. Following the terminology of Perry & Chong (1987) (see figure 16) the reduced system is written as

$$\begin{bmatrix} \dfrac{\mathrm{d}Q}{\mathrm{d}t} \\ \dfrac{\mathrm{d}R}{\mathrm{d}t} \end{bmatrix} = \begin{bmatrix} -2\kappa & -3 \\ 0 & -3\kappa \end{bmatrix} \begin{bmatrix} Q \\ R \end{bmatrix}. \tag{3.14}$$

Defining the second-rank tensor $\boldsymbol{B}$ as

$$\boldsymbol{B} = \begin{bmatrix} -2\kappa & -3 \\ 0 & -3\kappa \end{bmatrix}, \tag{3.15}$$

then, the invariants of this two-dimensional system (p and q) are

$$p = -\mathrm{trace}\,(\boldsymbol{B}) = 5\kappa, \tag{3.16}$$

$$q = \det(\boldsymbol{B}) = 6\kappa^2. \tag{3.17}$$

Therefore $q/p^2 = 6/25 < 1/4$ and $q > 0$ independently of the value of κ. Referring to figure 16, this result implies that solution trajectories for the system of differential equations given by (3.10) and (3.11) will have a topology of a stable node in the vicinity of the origin of the (Q, R)-plane.

The second critical point is located at the second root of the system

$$-3R - 2\kappa Q = 0, \tag{3.18}$$

$$\tfrac{2}{3}Q^2 - 3\kappa R = 0, \tag{3.19}$$

or ($Q = -3\kappa^2, R = 2\kappa^3$) which lies on the $R > 0$ branch of the $D = 0$ curve. This point can also be classified using the same ideas by first defining a coordinate translation

$$\widehat{Q} = Q + 3\kappa^2, \tag{3.20}$$

$$\widehat{R} = R - 2\kappa^3, \tag{3.21}$$

with the second critical point now lying at ($\widehat{Q} = 0, \widehat{R} = 0$). Substituting these new variables into equations (3.10) and (3.11) results in

$$\frac{d\widehat{Q}}{\mathrm{d}t} = -3\widehat{R} - 2\kappa\widehat{Q}, \tag{3.22}$$

$$\frac{\mathrm{d}\widehat{R}}{\mathrm{d}t} = \tfrac{2}{3}\widehat{Q}^2 - 3\kappa\widehat{R} - 4\kappa^2\widehat{Q}. \tag{3.23}$$

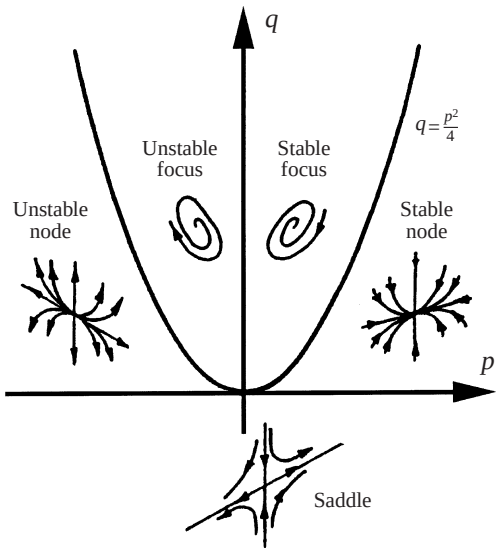

FIGURE 16. Summary of two-dimensional solution trajectories (from Perry & Chong 1987).

Proceeding as before, the invariants for the linear terms of this system can be easily computed and are given by

$$p = 5\kappa, \tag{3.24}$$

$$q = -6\kappa^2, \tag{3.25}$$

and, from figure 16, this corresponds to a saddle point for any value of κ.

Actual solution trajectories for the full nonlinear system given by equations (3.10) and (3.11) were computed numerically for two widely different values of κ: $\kappa = 0.1$ and $\kappa = 100$ which, from Cheng & Cantwell (1996) would correspond to high and low Reynolds number flows respectively. These trajectories are plotted in figure 17(a, b). For this calculation, solution trajectories were only initialized at points in (Q, R)-space where figure 2 indicates that actual turbulent data points exist. For the case of $\kappa = 100$ (i.e. low Reynolds number flow), the second critical point is located far to the right of the picture. Consequently the stable node geometry predicted near the origin becomes the dominant flow characteristic with a strong tendency for the data to evolve toward the origin of coordinates as shown in figure 17(b). For small values of κ (i.e. high Reynolds number) the saddle point moves closer to the origin ($Q = -0.03$, $R = 0.002$) and the trajectories show the combined character of both critical points as demonstrated in figure 17(a). Points with initially large positive D have a strong tendency to evolve toward $R > 0$ and the plot begins to approach the restricted Euler solution.

In the next sections, the validity of some of these assumptions is tested by computing the actual Lagrangian evolution of the invariants Q and R using the direct numerical simulation data and comparing it to the behaviour predicted here.

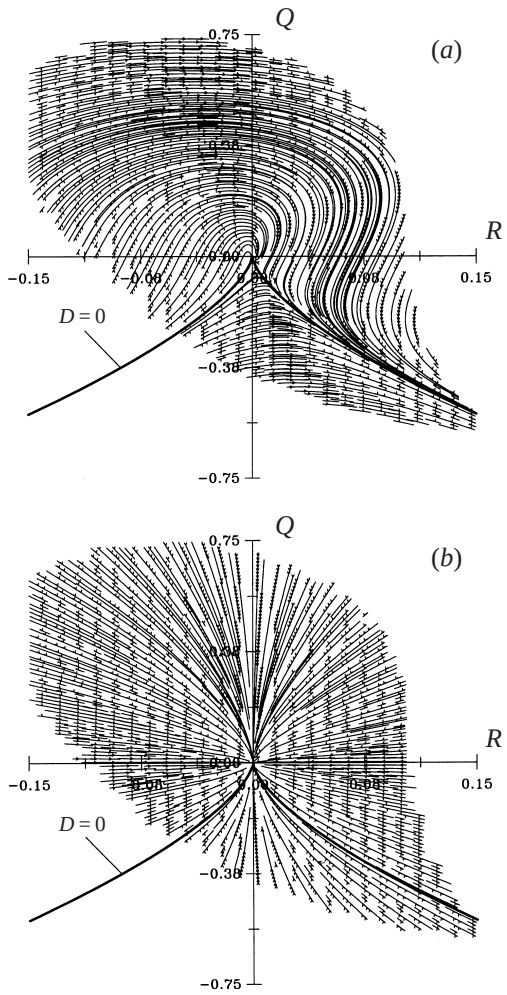

FIGURE 17. Lagrangian evolution trajectories in the (Q, R)-plane computed using the assumption $H_{ij} \sim -kA_{ij}$. (*a*) $\kappa = 0.1$. (*b*) $\kappa = 100$.

3.1. *Numerical method*

The motion of a fluid particle in a three-dimensional flow field is governed by the simple relation

$$\frac{\mathrm{d}\boldsymbol{x}}{\mathrm{d}t} = \boldsymbol{U}(\boldsymbol{x}, t), \tag{3.26}$$

which can be integrated in a straightforward manner. The main difficulty with this process is that, as time is advanced, the instantaneous particle position will, in general, not coincide with any of the direct numerical simulation Eulerian mesh points. Therefore, for every particle that is being followed, it is necessary to interpolate this Eulerian vector $\boldsymbol{U}(\boldsymbol{x}, t)$ to obtain the velocity at the particle's new position at the given time step. For a spectral DNS, the same series expansion used in the calculation could be used to interpolate the velocity field with no loss of accuracy. This approach is however far too expensive if a large number of fluid particles are being followed. On the other hand, Yeung & Pope (1988) as well as Rovelstad, Handler & Bernard (1994) carried out extensive studies of the effects of interpolation

errors on Lagrangian statistics of turbulence and concluded that lower-order schemes, like linear interpolation and cubic splines, yield unacceptable results. Therefore, the approach adopted here uses a mixed polynomial–spectral formula that is based on the methods proposed and validated by Kontomaris, Hanratty & McLaughlin (1992) and Balachandar & Maxey (1989). This interpolation formula uses Fourier series in the streamwise and spanwise directions (x and z) and Nth-order Lagrange polynomials in the wall-normal one (y) and is given by

$$U_r\left(x_\circ^n, y_\circ^n, z_\circ^n, t^n\right) = \sum_j \sum_{k_x} \sum_{k_z} \widehat{U}_r(k_x, y_j, k_z, t^n) \mathrm{e}^{\mathrm{i}k_x x_\circ^n} \mathrm{e}^{\mathrm{i}k_z z_\circ^n} \mathscr{L}_j\left(y_\circ^n\right), \tag{3.27}$$

where $\widehat{U}_r\left(k_x, y_j, k_z, t^n\right)$ are the two-dimensional Fourier coefficients for the rth component of the velocity vector, $(x_\circ^n, y_\circ^n, z_\circ^n)$ refer to the particle's position at time t^n and (x_i, y_j, z_k) is the time-independent Eulerian mesh. The Lagrange polynomials $(\mathscr{L}_j)$ were constructed by centring the interpolation stencil around the $y_\circ^n$-coordinate of each particle and using the standard formula

$$\mathscr{L}_j(y_\circ^n) = \prod_{\substack{i=j-N/2 \\ i\neq j}}^{j+N/2} \frac{\left(y_\circ^n - y_i\right)}{\left(y_j - y_i\right)}, \tag{3.28}$$

where N was set to 6. The integration of equation (3.26) was carried out using the following predictor-corrector set:

$$\boldsymbol{x}_* = \boldsymbol{x}_\circ^n + \Delta t \boldsymbol{U}\left(\boldsymbol{x}_\circ^n, t^n\right), \tag{3.29}$$

$$\boldsymbol{x}_\circ^{n+1} = \boldsymbol{x}_\circ^n + \frac{\Delta t}{2}\left\{\boldsymbol{U}\left(\boldsymbol{x}_\circ^n, t^n\right) + \boldsymbol{U}\left(\boldsymbol{x}_*, t^{n+1}\right)\right\}, \tag{3.30}$$

which is formally second-order accurate.

The accuracy of this scheme was tested by tracking forward a group of 5000 particles that were initially uniformly distributed on the computational domain. After about 55 steps (or $\Delta t u_\tau^2/\nu \approx 24$), the calculation was stopped and the particles were tracked backward in time for the same number of steps. A global measure of the error was computed by subtracting the positions of the particles in the return trajectories from their corresponding positions in the forward one and averaging over all particles. This is, after n steps

$$\varepsilon^n = \sum_{\text{particles}} \frac{|\boldsymbol{x}^n_{\text{forward}} - \boldsymbol{x}^n_{\text{backward}}|}{\text{number of particles}}. \tag{3.31}$$

Figure 18 shows the average error computed using equation (3.31) normalized using an estimate of the Taylor microscale λ as a function of non-dimensional time (tu_τ^2/ν). The microscale was estimated using classical scaling arguments regarding the production and dissipation terms in the TKE equation (see for example Tennekes & Lumley 1974, chapter 2) which yield

$$\lambda = \frac{\delta}{Re_\delta^{1/2}}, \tag{3.32}$$

where δ is the boundary layer thickness and $Re_\delta = U_\infty \delta/\nu$. As can be seen in the figure, after a forward integration time of $t^+ \approx 24$, the particles returned to within an average distance of less than 2λ of their initial starting location.

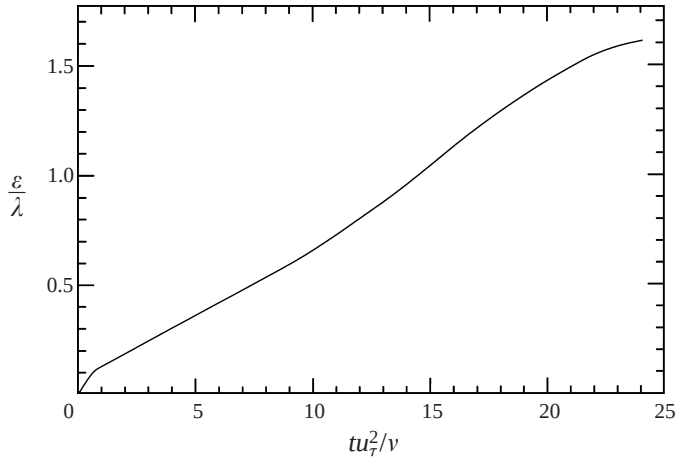

FIGURE 18. Global position error for an ensemble of 5000 fluid particles tracked forward and backward as a function of the non-dimensional forward integration time. The average error ε was normalized using an estimate of the Taylor microscale λ.

The study of the Lagrangian behaviour of the invariants was done by keeping track of the evolution of these scalars in the (Q, R)-plane and was done in the following manner: fluid particles were collocated with the Eulerian DNS grid and were followed for one simulation time step while keeping track of the change in the values of Q and R. With these data, it was possible to compute a pseudo-velocity vector for the Lagrangian evolution of tensor invariants in the (Q, R)-plane. This vector is defined as

$$\boldsymbol{W} = \frac{\mathrm{D}R}{\mathrm{D}t}\hat{\boldsymbol{i}} + \frac{\mathrm{D}Q}{\mathrm{D}t}\hat{\boldsymbol{j}}, \tag{3.33}$$

and it allows the construction of evolution trajectories in the (Q, R)-plane. After this another set of particles, starting again on the DNS grid, were picked and followed for one time step. This process was repeated in over 50 DNS flow realizations which yielded a sample of over 15 million particles. Mean results were obtained by dividing the (Q, R)-plane into 16 000 bin cells and ensemble averaging over all the data points that fell into each bin.

The calculations just described involved a significant amount of high-order interpolation of the three-dimensional velocity field and, therefore, necessitated a large amount of computer CPU time. For the particular interpolation scheme chosen here, the computational cost was of order MN^2 per time step (where M is the number of fluid particles being followed and N is the number of grid points in the simulation). Therefore, in order to limit the computer resources required, the results shown next were obtained for a simulation with a Reynolds number $Re_\theta = 300$.

3.2. *Time evolution of the invariants of the velocity gradient tensor*

Figure 19 shows the time-averaged Lagrangian evolution trajectories of the Q and R invariants in the (Q, R)-plane. The view showed is for the entire boundary layer. The figure bears a striking resemblance to the results shown in figure 17(*b*) (low Reynolds number case) and shows a clear tendency for fluid particles to move toward the origin of coordinates in the (Q, R)-plane. This tendency is of course also consistent with the probability distributions shown in figure 2 which indicates that most of the data points are gathered near the origin. Also, the presence of two asymptotes is

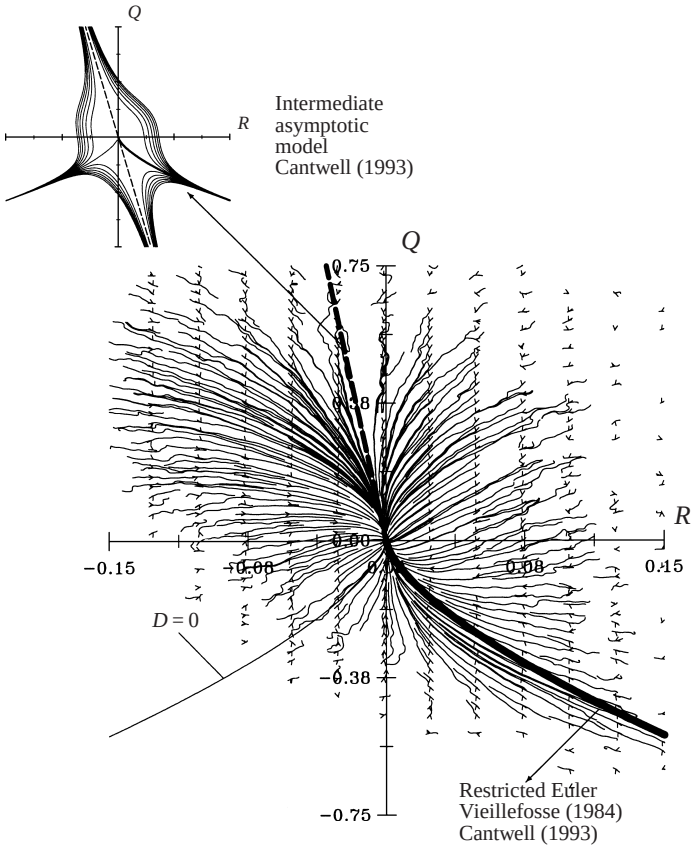

FIGURE 19. Time-averaged particle trajectories in the (Q, R)-plane at $Re_\theta = 300$. The dashed line is an asymptote of the form $R + fQ + f^3 = 0$ with $f = 0.043$

apparent in the trajectory diagram. The first one is the $D = 0$ curve. This is the line that separates the regions where the velocity gradient tensor has complex eigenvalues from those where the eigenvalues are real. This particular asymptote is clearly visible in the lower-right quadrant where the particle paths seem to follow that curve toward the origin. Recall that this calculation is for $Re_\theta = 300$ and one would expect, on the basis of the earlier discussion, that at higher Reynolds number, the trajectories may instead begin to resemble those shown in figure 17(*a*). See for comparison figure 12 of Ooi *et al.* (1999) where the evolution of Q and R is studied in a simulation of isotropic turbulence at $Re_\lambda = 70.9$.

Cantwell (1992) constructed exact solutions for the behaviour of the velocity gradient tensor and its invariants under the assumption of $H_{ij} = 0$ which corresponds to the case $\kappa = 0$ discussed earlier (see equations (3.3), (3.4), (3.5) and (3.6)). Even with the limitations imposed by this idealization, Cantwell (1992) observed that some of the features of those solutions had also been observed in direct numerical simulations of turbulence and, on that basis, it is possible that this simplified model might be useful in explaining some of the mechanisms that govern the evolution of the small-scale motion, particularly in the inertial subrange. One of the features of this model is that the discriminant is a materially conserved quantity and fluid particles will evolve, in time, toward the lower-right quadrant of the (Q, R)-plane. This trend can also be observed in the evolution trajectories shown in figure 19 in that the particles in the

lower-right quadrant tend toward the $D = 0$ curve. In the restricted Euler model, these particles evolve toward an asymptotic state in which their rate-of-strain tensors (S_{ij}) have two positive and one negative eigenvalues and their vorticity vectors are exactly aligned with the intermediate eigenvector of S_{ij}. However, not enough flow field information was obtained to verify whether this behaviour was also present in the particles in the lower-right quadrant of figure 19. This issue remains an important topic for future work as it suggests the existence of some universal characteristics for the motions of the inertial subrange.

The second asymptote seems to be a straight line (indicated by the dashed line in figure 19) that starts near the origin and extends into the upper-left quadrant (stable focus–stretching). The tendency of the trajectories toward this line is also consistent with the shape of the probability distribution for Q and R in that the contours of equal probability seem to lean over into that upper-left region. Cantwell (1993) also studied the evolution of the velocity gradient tensor under the relaxed assumption of $H_{ij} \neq 0$ (but without assuming the behaviour $H_{ij} \sim -\kappa A_{ij}$) and postulated the existence of an intermediate asymptotic state where the angular momentum of fluid elements changes slowly. In that argument, it was hypothesized instead that A_{ij} evolves according to the simple model

$$A_{ij}(t) = M_{ij} \exp\left[\int f(t)\,\mathrm{d}t,\right] \tag{3.34}$$

$$\frac{\mathrm{D}A_{ij}}{\mathrm{D}t} = A_{ij} f(t), \tag{3.35}$$

where M_{ij} is a constant matrix and $f(t)$ is a scalar function of time. Under those assumptions it can be shown that Q and R should evolve toward a region of attraction near ($Q = 0$, $R = 0$). One feature of this model is the existence of an asymptote of the form

$$R + fQ + f^3 = 0, \tag{3.36}$$

with f = constant (i.e. a straight line in the (Q, R)-plane). In figure 19, the value $f = 0.043$ was used to draw the dashed line shown. Cantwell (1993) also pointed out that, under those assumptions about the form of A_{ij}, flow patterns that conform to equation (3.36) should be typical features of the flow. Such structures would also have the property that, although the invariants may vary widely within the volume where $D > 0$, the real eigenvalue within this volume is approximately constant.

Another important observation is that, with the exception of the small fraction of trajectories that start in the upper-right quadrant (unstable focus–compression) and cross over into the upper-left one (stable focus–stretching) toward the second asymptote, the predominant time-averaged tendency is for fluid elements to evolve retaining their topological classification. The computer visualization of the flow also confirmed this tendency.

As was mentioned, figure 19 shows an ensemble average of particles from the entire boundary layer. In order to look at the effects of the inhomogeneity of the flow, the computation was repeated while keeping track of the particles' wall-normal position. Figure 20(*a–d*) shows the results of that computation as a function of y^+. The most striking departure from the overall features observed in figure 19 is seen in the viscous sublayer (figure 20*a*). There is still a visible tendency for the fluid particles to move toward the origin in the (Q, R)-plane but, as can be seen, they do so following a set of clockwise-turning spiral patterns that show no sign of the asymptotic behaviour that was previously mentioned. Using the same nomenclature shown in figure 16, these

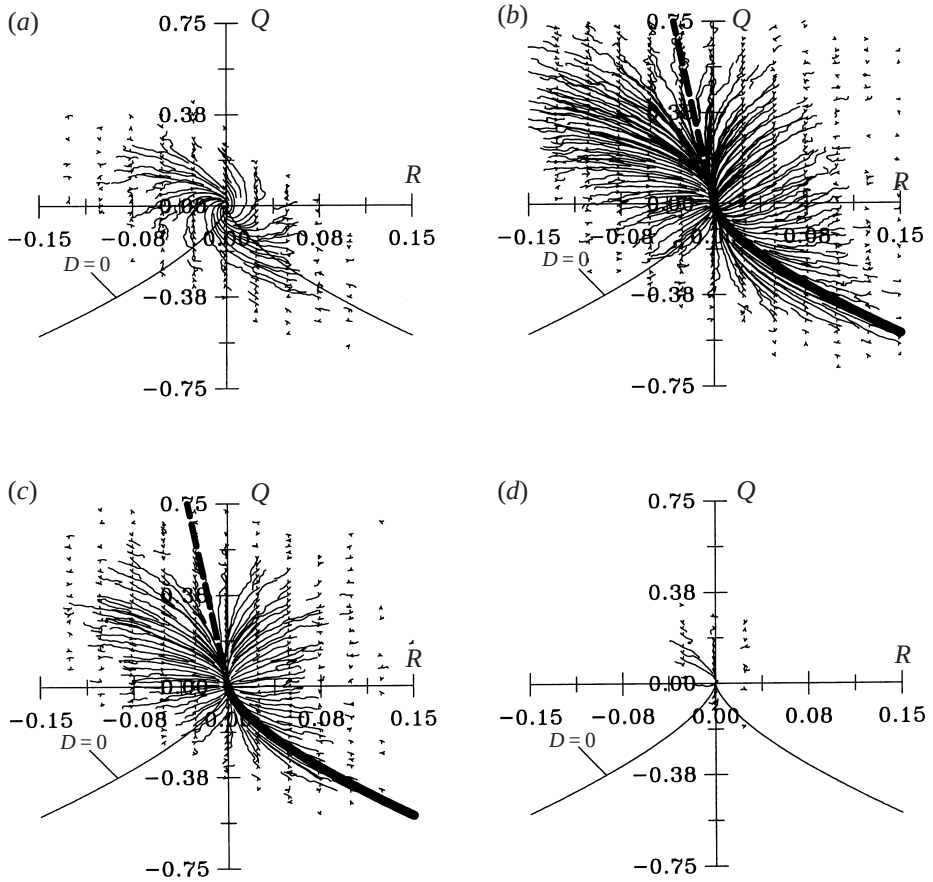

FIGURE 20. Time-averaged particle trajectories in the (Q, R)-plane at $Re_\theta = 300$ as a function of distance from the wall. (*a*) $y^+ < 5.6$, (*b*) $5.6 < y^+ < 41$, (*c*) $41 < y^+ < 105$, (*d*) $y^+ > 105$.

trajectories now have a stable focus topology which also implies that, very near the wall, the assumption of $H_{ij} \sim -\kappa A_{ij}$ no longer holds. In studying the solution of the restricted Euler model, Cantwell (1992) suggested that such asymptotic behaviour, if it exists at all in real turbulence, is unlikely to be found at the dissipative scales of the flow since the effects of viscosity are important at those fine scales. Figure 20(*a*) is consistent with that argument. Even accounting for the decay of the turbulence as the wall is approached, the motions that produced that picture are those with the smallest, most dissipative scales in this flow and restricted Euler-type behaviour cannot be seen in it. Similarly, the largest eddies in the flow are characterized by relatively low gradients of velocity and, consequently, could not have produced the range of values for the invariants that can be observed in figures 20(*b*) and 20(*c*). Therefore the behaviour suggested by the restricted Euler solution is most likely to be a property of the intermediate scales of the flow.

Further away from the wall, in figures 20(*b*) (buffer region) and 20(*c*) (logarithmic layer), the patterns exhibit the same characteristics described before for figure 19. Moving away from the viscosity-dominated sublayer, and as the level of turbulence intensifies, the trajectories acquire a node-like shape as predicted earlier for low Reynolds number flows and the aforementioned asymptotes become clear. As was the case for the joint probability distributions of Q and R, the only obvious difference

between the plots for the buffer and the log region seems to be in the scale which is a direct consequence of the range of velocity gradients in those regions of the flow. Figure 20(*d*) shows the results for the wake region where the decreasing level of the turbulence associated with the reduced mean shear make the figure relatively featureless. Nonetheless, close inspection of the trajectories still reveals a tendency toward the origin of coordinates in a node pattern.

4. Conclusions

At any point in a three-dimensional flow field, the local flow pattern is determined by the combined effects of the rotation rate and the irrotational strain rate. The balance between these two factors establishes the shape of the instantaneous streamlines. The invariants of the velocity gradient tensor provide a quantitative measure of that balance and hence an unambiguous framework for the description of turbulent flows. From these invariants, the cubic discriminant (equation (1.3)) emerged as a scalar flow marker that can be used effectively for the study of the structure of turbulence. This methodology has the added advantage of being independent of the frame of reference used, in principle does not require the setting of an arbitrary threshold and it is directly applicable to any incompressible flow. The method can also be readily extended to compressible cases.

The physical picture of near-wall structure constructed using the discriminant indicates that regions where the rate of rotation determines the local fluid motion (positive discriminant) form large-scale, coherent, connected flow structures. These eddies consist mainly of intertwined streamwise tubes that extend from the beginning of the wake region all the way down very close to the wall. Embedded among these tubes, a small number of hairpin-shaped structures of various sizes were also visible. This picture is consistent with the idea of attached eddies as first suggested by Theodorsen (1955) and Townsend (1956) and complements the views of near-wall turbulence structure of Kline *et al.* (1967). These large-scale structures are highly correlated with motions with high instantaneous values of Reynolds shear stress ($u'v'$), turbulent kinetic energy and dissipation. These regions, characterized by a rapid change of sign of the discriminant, seem to illustrate what Townsend (1956) once described as active and inactive turbulence. It is interesting to notice that the most active motions in terms of $u'v'$ were preferentially located in regions where the flow pattern indicated that vortex tubes are being locally compressed (the velocity gradient tensor has two complex and one real, negative eigenvalue). For these same regions, equation (2.7) indicates that the pressure field cannot reach a local minimum since $\nabla^2 p > 0$ is a necessary condition for such an extremum to occur. In fact, the pressure could reach a local maximum which suggests the possibility of a vortex breakdown-like mechanism for these events.

The evolution trajectories shown in figure 19 indicate the existence of two different asymptotic states for the velocity gradient tensor which may allow the identification of certain universal characteristics of fine-scale turbulence. They also suggest that, at least in some regions or at the level of these small scales, the evolution of the velocity gradient tensor could be modelled using simplified schemes. The two models for the asymptotic behaviour as well as the assumption of $H_{ij} \sim -\kappa A_{ij}$ predict a monotonic Lagrangian evolution of the velocity gradients and cannot fully account for all the features observed in the stationary shape of the PDF of the invariants. In statistically steady flows, like the one studied here, this monotonic evolution is interrupted by events involving the production and dissipation of turbulent kinetic

energy. Furthermore this process is likely to be modulated by the large scales and hence it may be different for different flows. Neither model includes specific information about the boundary conditions of the flow. For the motions in the lower-right quadrant of the (Q, R)-plane (the tail of the distribution) that asymptote toward the $D = 0$ line, this is probably adequate. These are the smallest-scale motions in the flow and, as such, one would expect that only their scales – and neither their shapes nor their character – would vary among different flows and Reynolds numbers. This in fact seems to be the case in all the different flows studied thus far using this method. One would not expect such insensitivity to boundary conditions to apply to the asymptote that extends into the upper-left quadrant. These are the stretched vortex tubes that form parts of the large-scale structures visualized in figure 3 and are likely to be dependent on boundary and initial conditions. While all the flows studied to date seem to have a preference for these kinds of flow patterns, the specific shape and strength of the asymptote vary somewhat. They seem for instance to be much more pronounced in the plane, time-developing mixing layer of Moser & Rogers (1993) studied by Soria *et al.* (1994) than in the present boundary layer flow. The intermediate asymptotic model leaves open the possibility of accounting for these factors in the matrix M_{ij} and the function $f(t)$ in equations (3.34) and (3.35). This would be an useful topic for further research.

Finally, the relationship between the invariants of the velocity gradient tensor and the Reynolds stresses may prove useful in the context of the modelling of turbulence. In applications such as subgrid-scale models for large-eddy simulations, the unresolved stresses are usually assumed to depend only on the symmetric rate-of-strain tensor (S_{ij}). The peculiar double-peak shape of figure 7 (as well as relations like equation (2.3)) suggest that it is the relative balance between the rotation and the strain rates that determines the magnitude of Reynolds stress generating events.

The authors would like to express their sincere appreciation to Dr P. Spalart who graciously provided us with the direct numerical simulation code from which these results were obtained.

This work was supported in part by NASA Ames-Stanford Joint Institute for Aeronautics and Acoustics grant NCC2-55 and NASA Langley grant NAG-1-1610. Computer flow visualization facilities were provided by the Large-Scale Interactive Visualization Environment (LIVE) at the NASA Ames Research Center.

REFERENCES

Balachandar, S. & Maxey, M. R. 1989 Methods for evaluating fluid velocities in spectral simulations of turbulence. *J. Comput. Phys.* **83**, 96–125.

Bernard, P. S., Thomas, J. M. & Handler, R. A. 1993 Vortex dynamics and the production of Reynolds stress. *J. Fluid Mech.* **253**, 385–419.

Blackburn, H. M., Mansour, N. N. & Cantwell, B. J. 1996 Topology of fine-scale motions in turbulent channel flow. *J. Fluid Mech.* **310**, 269–292.

Brooke, J. W. & Hanratty, T. J. 1993 Origin of turbulence-producing eddies in a channel flow. *Phys. Fluids* A **5**, 1011–1022.

Cantwell, B. J. 1992 Exact solution of a restricted Euler equation for the velocity gradient tensor. *Phys. Fluids* A **4**, 782–793.

Cantwell, B. J. 1993 On the behavior of the velocity gradient tensor invariants in direct numerical simulations of turbulence. *Phys. Fluids* A **5**, 2008–2013.

Chacin, J. M. & Cantwell, B. J. 1997 Study of turbulent boundary layer structure using the invariants of the velocity gradient tensor. *TF Rep.* 70. Department of Mechanical Engineering, Stanford University.

Chacin, J. M., Cantwell, B. J. & Kline, S. J. 1996 Study of turbulent boundary layer structure using the invariants of the velocity gradient tensor. *Expl Thermal Fluid Sci.* **13**, 308–317.

Chen, J. H., Chong, M. S., Soria, J., Sondergaard, R., Perry, A. E., Rogers, M., Moser, R. & Cantwell, B. J. 1990 A study of the topology of dissipating motions in direct numerical simulations of time-developing compressible and incompressible mixing layers. *Proc. Summer Program, Center for Turbulence Research, Stanford University*, pp. 139–161.

Cheng, W. & Cantwell, B. J. 1996 Study of the velocity gradient tensor in turbulent flow. *JIAA Tech. Rep.* 114. Department of Aeronautics and Astronautics, Stanford University.

Chong, M. S., Perry, A. E. & Cantwell, B. J. 1990 A general classification of three-dimensional flow fields. *Phys. Fluids* A **2**, 765–777.

Chong, M. S., Soria, J., Perry, A. E., Chacin, J., Cantwell, B. J. & Na, Y. 1998 Turbulence structures of wall-bounded shear found using DNS data. *J. Fluid Mech.* **357**, 225–247.

Head, M. R. & Bandyopadhyay, P. 1978 Combined flow visualization and hot wire measurements in turbulent boundary layers. In *Lehigh Workshop on Coherent Structure in Turbulent Boundary layers*, pp. 98–125.

Jeong, J. & Hussain, F 1995 On the identification of a vortex. *J. Fluid Mech.* **285**, 69–94.

Kline, S. J., Reynolds, W. C., Schraub, F. A. & Runstadler, P. W. 1967 The structure of turbulent boundary layers. *J. Fluid Mech.* **30**, 741–773.

Kontomaris, K., Hanratty, T. J. & McLaughlin, J. B. 1992 An algorithm for tracking fluid particles in a spectral simulation of turbulent channel flow. *J. Comput. Phys.* **103**, 231–242.

Loulou, P. 1996 Direct numerical simulation of incompressible pipe flow using a B-spline spectral method. PhD Dissertation, Department of Aeronautics and Astronautics, Stanford University.

Martin, J. & Dopazo, C. 1995 Velocity gradient invariant evolution from a linear diffusion model. In *Proc. Twelfth Australasian Fluid Mechanics Conf.*, pp. 743–746.

Meinhart, C. D. & Adrian, R. J. 1995 On the existence of uniform momentum zones in a turbulent boundary layer. *Phys. Fluids* **7**, 694–696.

Miyake, Y. & Tsujimoto, K. 1996 Behavior of quasi-streamwise vortices in near-wall turbulence. *Proc. 1996 ASME Fluids Engineering Division Summer Meeting*. Part 3, pp. 41–48.

Moser, R. & Rogers, M. 1993 The three-dimensional evolution of a plane mixing layer: pairing and transition to turbulence. *J. Fluid Mech.* **247**, 275–320.

Na, Y. & Moin, P. 1996 Direct numerical simulation of turbulent boundary layers with adverse pressure gradient and separation. *TF Rep.* 68. Department of Mechanical Engineering. Stanford University.

Ooi, A., Martin, J., Soria, J. & Chong, M. 1999 A study of the evolution and characteristics of the invariants of the velocity-gradient tensor in isotropic turbulence. *J. Fluid Mech.* **381**, 141–174.

Perry, A. E. & Chong, M. S. 1987 A description of eddying flow patterns using critical-point concepts. *Ann. Rev. Fluid Mech.* **19**, 125–155.

Robinson, S. K. 1990 Kinematics of turbulent boundary layer structure. PhD Dissertation, Department of Mechanical Engineering, Stanford University.

Rovelstad, A., Handler, R. A. & Bernard, P. S. 1994 The effect of interpolation errors on the Lagrangian analysis of simulated turbulent channel flow. *J. Comput. Phys.* **110**, 190–195.

Schwartz, S. P. & Smith, C. R. 1983 Observation of streamwise vortices in the near-wall region of a turbulent boundary layer. *Phys. Fluids* **26**, 641–652.

Soria, J., Sondergaard, R., Cantwell, B. J., Chong, M. S. & Perry, A. E. 1994 A study of the fine-scale motions of incompressible time-developing mixing layers. *Phys. Fluids* **6**, 871–884.

Spalart, P. R. 1988 Direct simulation of a turbulent boundary layer up to $Re_\theta = 1410$. *J. Fluid Mech.* **187**, 61–98.

Tennekes, H & Lumley, J. L. 1974 A first course in turbulence. 1st Edn. MIT Press.

Theodorsen, T. 1955 The structure of turbulence. In *50 Jahre Grenzschichtforsung* (ed. H. Görtler & W. Tollmein), pp. 55–62. Braunschweig, Vieweg & Sohn.

Townsend, A. A. 1956 *The Structure of Turbulent Shear flow*, 1st Edn. Cambridge University Press.

Vieillefosse, P. 1984 Internal motion of a small element of fluid in an inviscid flow. *Physica* A **150**, 150–162.

Wallace, J. M., Eckelmann, H. & Brodkey, R. S. 1972 The wall region in turbulent shear flow. *J. Fluid Mech.* **54**, 39–48.

Yeung, P. K. & Pope, S. B. 1988 An algorithm for tracking fluid particles in numerical simulations of homogeneous turbulence. *J. Comput. Phys.* **79**, 373–416.